Article

Single-step laser-printed integrated sulfur cathode toward high-performance lithium−sulfur batteries

Rongliang Yang [1], Yi Chen[1], Yexin Pan[1], Minseong Kim[1], Huan Liu [1], Connie Kong Wai Lee[1], Yangyi Huang[1], Aidong Tang [2,3], Feiyue Tu[4], Tianbao Li[4] & Mitch Guijun Li [1] ✉

Lithium−sulfur batteries are expected to supersede existing lithium-ion batteries due to the high theoretical energy density of sulfur cathodes (positive electrodes). Unfortunately, inefficient redox reactions and the "shuttle effect" hinder their commercial development. Assembling high-performance nanostructured sulfur host materials into a sulfur cathode presents a viable solution. However, fabricating host materials and preparing sulfur cathodes involve complicated, multistep, and labor-intensive processes under varying temperatures and conditions, raising concerns about efficiency and cost in practical production. Herein, we propose a single-step laser printing strategy to prepare high-performance integrated sulfur cathodes. During the high-throughput laser-pulse irradiation process, the precursor donor is activated, producing jetting particles that include in-situ synthesized halloysite-based hybrid nanotubes, sulfur, and glucose-derived porous carbon. After laser printing, a composite layer, containing host materials, active materials, and conductive components, is uniformly coated onto a carbon fabric acceptor, forming an integrated sulfur cathode. The laser-printed sulfur cathodes exhibit high reversible capacity and low capacity attenuation during cycling measurements. Furthermore, the laser-printed high-loading samples show high performance in both coin and pouch lithium−sulfur cells. This strategy would simplify the fabrication process in lithium−sulfur battery industry and inspire advancements in other battery research.

The growing energy demands of modern society have made rechargeable batteries a critical research subject. Thus, researchers have been making significant efforts to develop high-energy-density rechargeable batteries that surpass current commercial lithium-ion batteries[1–4]. Among the existing options, lithium-sulfur (Li−S) batteries are strong contenders[5–7]. However, several intricate issues still impede the widespread application of Li−S batteries. The nearly dielectric nature of sulfur and polysulfides limits the high-rate performance of Li−S batteries, particularly at high sulfur loadings. During redox reactions, the active materials (from elemental sulfur to polysulfides) undergo significant volume changes, which can lead to irreversible structural changes in the electrode. Long-chain soluble polysulfides cause the "shuttle effect,"

---

[1]Center for Smart Manufacturing, Division of Integrative Systems and Design, The Hong Kong University of Science and Technology, Clear Water Bay, Kowloon, Hong Kong SAR, China. [2]College of Chemistry and Chemical Engineering, Central South University, Changsha, China. [3]Engineering Research Center of Nano-Geomaterials of Ministry of Education, China University of Geosciences, Wuhan, China. [4]Changsha Research Institute of Mining and Metallurgy Co. LTD, Changsha, China. ✉e-mail: mitchli@ust.hk

resulting in the deposition of Li₂S on the lithium anode (negative electrode) and the subsequent loss of active sulfur species. The conversion between elemental sulfur (S_8) and Li_2S involves several sluggish redox processes[8], leading to low-rate capacity.

One promising approach for improving the performance of Li–S batteries is to create an efficient sulfur cathode (positive electrode) to mitigate the shuttle effect and expedite the evolution of sulfur species[9–11]. Host materials exhibiting strong polysulfide-absorbing properties or high acceleration for lithium polysulfide (LiPS) transformation are critical components in a practical sulfur cathode. Promising host materials include MnO_2[12,13], VN[14], ZnO[15], ZnSe[16], MoS_2[17–19], NiCo-LDH[20], MXene[21,22], etc. Researchers typically design 3D nano-/micro-structures in these host materials to increase their effective active area. For instance, $Fe_{3−x}C@C$ hollow microspheres have been synthesized as sulfur host materials to increase the number of active interfaces for sulfur redox reactions[23]. $Fe_3O_{4−x}$/FeP-modified carbon tubes have been fabricated to restrain sulfur dissolution and increase active sites, contributing to a high capacity of 7.2 mAh cm⁻² in Li–S batteries[24]. Unfortunately, most of these high-performance host materials require complex and costly synthetic routes (e.g., solvothermal synthesis, vapor chemical deposition, etc.), raising concerns about their scalable fabrication. In recent years, various clay minerals with natural nanostructures have attracted the attention of Li–S battery researchers. These nanostructured clays can be directly used as sulfur hosts or structural components in a sulfur cathode, considerably reducing manufacturing costs. Shao et al. fabricated a 2D montmorillonite-based heterostructure (MMT-RGO) to promote the diffusion and evolution of polysulfides, resulting in a high battery capacity of 1317 mAh g⁻¹ at 0.2[25]. Yang et al. developed a TiO_2-doped halloysite nanotube to accelerate polysulfide evolution, enhancing cycling performance in Li-S batteries[26]. However, the low conductivity of nanoclays leads to low electronic switching efficiency during charging and discharging, necessitating the inclusion of conductive additives to enhance the conductivity of a clay-based cathode.

Areal sulfur loading is a critical parameter for meeting the demands of commercial electronic portable devices[27]. Typically, a high-sulfur-loading Li–S battery provides high areal capacity. However, the high sulfur loading can lead to decreased electronic conductivity and an anabatic shuttle effect in batteries. There is a noteworthy trade-off between sulfur loading and areal capacity. Many reported Li–S cathodes have shown high mass-specific capacities over the last decade. However, most of these cathodes deliver sulfur loadings of less than 2 mg cm⁻² and areal capacities of less than 2 mAh cm⁻²[28,29]. In traditional tape-casting sulfur cathodes, high sulfur loading usually results in increased cathode thickness, leading to longer ion- and electron-transport pathways and reduced charge storage efficiency. In addition, the tremendous volumetric change of sulfur species in a thick cathode can cause high-probability active material shedding during operation. In this case, many researchers have attempted to fabricate various porous sulfur cathodes. For example, a porous carbon nanotube film has been identified as a good current collector for sulfur cathodes, contributing to a low capacity decrease rate of 0.03% over 1000 cycles[30]. However, transitioning from high-performance nanostructured energy storage units to macroscopic three-dimensional energy storage electrodes is not a straightforward physical accumulation. The structural design of host materials, the sulfur loading process, and the assembly of porous cathodes are all essential topics that require further study.

In this work, we develop a fast, convenient, and high-throughput single-step laser-induced synthesis process to fabricate an integrated sulfur cathode. Under the irradiation of a nanosecond pulse laser, manganese oxide nanoparticles are in-situ synthesized on the walls of halloysite nanotubes, forming homogeneous manganese oxide–doped halloysite nanotubes (MnO_x-Hal). The modified halloysite nanotubes, sulfur, and glucose-derived porous carbon form a uniform mixture coated on the carbon fibers. The resulting L-MnO_x-Hal-S@CF ('L' represents laser-printed, 'S' represents sulfur species, and 'CF'

represents carbon fabric) shows adjustable sulfur loading when tuning the sulfur content in the precursor donor layers. The laser-printed sulfur cathodes exhibit a high initial capacity (1215 mAh g⁻¹ at 0.2 C) and a low capacity decline of 0.02% per cycle over 1000 cycles at 1 C. Furthermore, the high-loading sulfur cathode (with sulfur content up to 7.8 mg cm⁻²) delivers a high residual capacity of 5.60 mAh cm⁻² in the 100th cycle (at 0.2 C). Therefore, this research presents a one-step approach to fabricate integrated high-loading sulfur cathodes.

Results

Laser printing for the one-step fabrication of sulfur cathodes

Figure 1a illustrates the laser printing process for the one-step fabrication of sulfur cathodes. This process is driven by a commercial desktop fiber laser scribing machine under an argon atmosphere. It can be easily integrated with automatic manufacturing systems, such as a robotic arm displacement system. The target materials are transferred from the precursor donor layer to the carbon fabric acceptor under laser irradiation. As proved in classical laser experiments[31–33] and our earlier study[34,35], a high-frequency pulse laser can be rapidly absorbed by the donor, generating high transient heat. According to the classical theory of laser–material interaction[32,33], the temperature rises inside the donor layer (ΔT) can be theoretically calculated as a function of the irradiated donor depth (z), the radial distance from the irradiated center (r), and irradiation time (t):

$$\Delta T(r,z,t) = \frac{I_{max}\gamma\sqrt{\kappa}}{\sqrt{\pi}K} \int_0^\tau \frac{p(\tau-t)}{\sqrt{t}\left[1+\frac{8\kappa t}{W^2}\right]} \exp\left[-\frac{z^2}{4\kappa t} - \frac{r^2}{4\kappa t + 0.5W^2}\right] dt,$$

(1)

where I_{max} (W m⁻²) is the maximal pulse intensity, γ is the light absorbance ratio of the material, κ (m² s⁻¹) is the material's thermal diffusivity, K (W K⁻¹ m⁻¹) is the thermal conductivity, τ (s) is the pulse width, and W (m) is the laser beam's mode field radius. Here, Eq. (1) is simplified to estimate the temperature distribution within different donor depths at the irradiated center ($r = 0$). The pulse intensity with temporal function $p(t)$ can be considered a constant value. Since most of the components in the donor are sulfur, the material's light absorptivity (for 1064 nm laser), thermal diffusivity, and thermal conductivity can be approximated as those of solid sulfur.

According to the simplified function, the temperature distribution profile in the donor versus donor depth is shown in Supplementary Fig. S1. The calculated theoretical temperature rise at the irradiation point can reach over 2×10^4 K. However, this theoretical temperature quickly drops with increasing donor depth, decreasing to zero at a depth of ~0.7 μm. The temperature in the irradiated donor layer (within 0.4 μm) is significantly higher than the boiling point of sulfur (718 K) and the decomposition temperature of $Mn(NO_3)_2$ (~473 K). This portion of the precursor donor is vaporized or decomposed into gas, generating a micro-explosion that promotes jetting formation (as illustrated in Fig. 1b on the left). Considering the average donor thickness is around 100–300 μm, the transiently vaporized precursor constitutes only a small fraction of the entire donor. The remainder is jetted from the donor slide, forming a jetting particle stream. Due to the high transient heating, intense plasma generates the jetting (shown on the right side of Fig. 1a and in Supplementary Movie 2). The heat generated during irradiation continues to diffuse inside the jetting particles. These particles undergo a complex transient heating and cooling process. Similar to other traditional thermochemical processes, the decomposed particles recombine into new materials during this concentrated thermal process. Some reports have demonstrated that unique materials can be synthesized using this laser-induced transient heating[36–39]. In this research, we designed and prepared a precursor layer containing sulfur (80 wt%), halloysite nanotubes (5 wt%), manganous nitrate (10 wt%), and glucose (5 wt%).
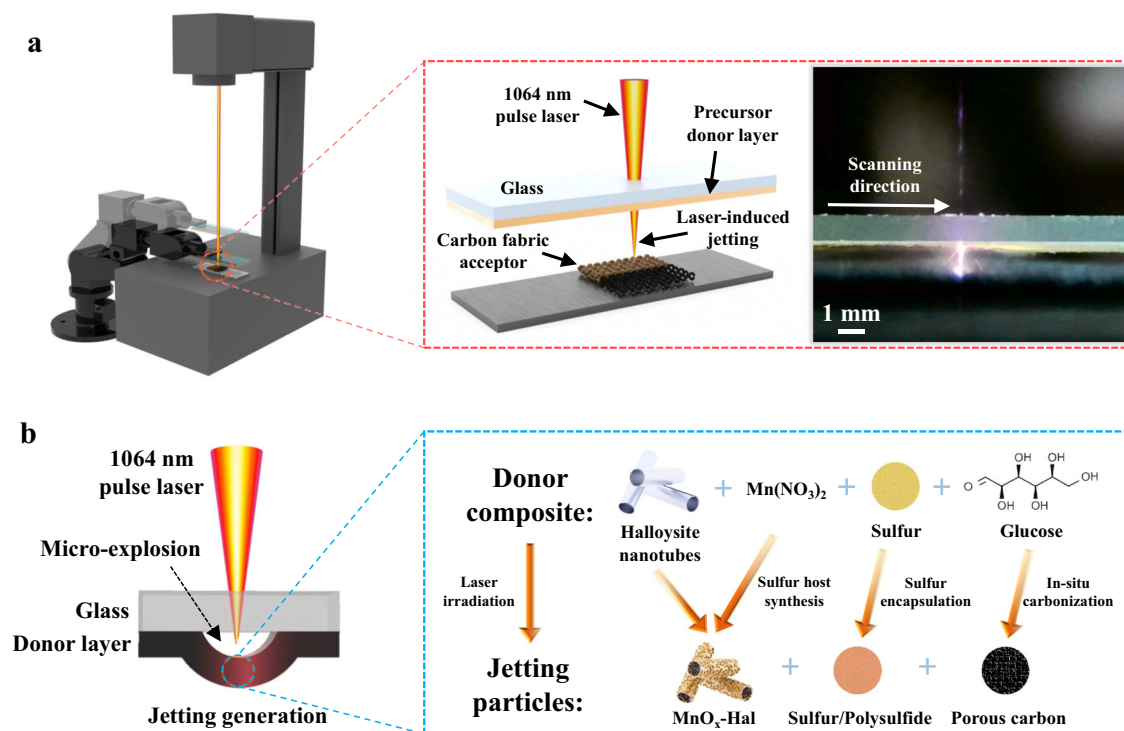
Fig. 1 | Schematic of the laser printing process. a Illustration of the single-step laser printing process for fabricating L-MnOx-Hal-S@CF cathode. Here, 'L' represents laser-printed, 'MnOx-Hal' represents manganese oxide–doped halloysite nanotubes, 'S' represents sulfur species, and 'CF' represents carbon fabric. The laser scribing machine is integrated with a robot arm displacement system. The right part shows the microscope view of the laser printing process. **b** Illustration of the micro-explosion and jetting generation process. The right part illustrates the material conversion during the concentrated thermal process.

The halloysite nanotube ($Al_2O_3 \cdot 2SiO_2 \cdot 4H_2O$), a clay mineral with a natural nanotube structure, is used as the structural material in the donor layer and the final printed product. Due to the adsorption properties of the nanotube structure, the halloysite nanotube aids in forming uniform precursor donors during the preparation process. In addition, owing to the high heat resistance of clay minerals, the nanotube structure remains stable during laser printing. After laser printing on the acceptor, the halloysite nanotube can act as a structural material for supporting the sulfur species and enhancing electrolyte infiltration during battery operation. Since materials with complex 3D nanostructures are hard to synthesize during the concentrated thermal process in laser printing, halloysite with a natural nanotube structure and high heat resistance is a good choice as a structural material. Furthermore, manganous nitrate and glucose are used to generate manganese oxide as the sulfur host material and porous carbon as conductive components, respectively. The concentrated thermal process can rapidly decompose both manganous nitrate and glucose. Instead of directly adding prefabricated host materials and conductive materials to the donor, using these precursors can help generate a uniformly distributed composite layer that combines sulfur, host materials, and conductive components. As illustrated on the right side of Fig. 1b, during laser irradiation, the manganous nitrate in the donor decomposes and is in situ transformed into manganese oxide nanoparticles on the walls of halloysite nanotubes, forming the homogeneous manganese oxide–doped halloysite nanotubes (MnOx-Hal). The glucose decomposes into porous carbon in situ. Meanwhile, most sulfur gets physically or chemically bonded with the generated host materials and conductive components during the laser process. These laser-activated particles are jetted from the donor under a laser-induced micro-explosion and rapidly transferred onto the carbon fabric acceptor. With the pulse laser scanning the donor, all donor materials are activated into jetting particles and rapidly transferred onto the carbon fabric acceptor.

Notably, the laser printing process for fabricating sulfur cathodes is a strategy that integrates sulfur host synthesis, sulfur encapsulation, and cathode fabrication into a single approach. In traditional manufacturing routes, these processes are conducted separately, requiring different processing temperatures and environments. For instance, sulfur host materials are typically synthesized using solvothermal methods, thermal annealing, or chemical vapor deposition at high temperatures (usually hundreds of degrees centigrade). Sulfur encapsulation is generally performed using the melting-diffusion method at 155 °C. Meanwhile, the sulfur cathode is generally fabricated by tape-casting method at processing temperatures below 100 °C. These processes consume energy, time, and auxiliary materials (e.g., solvents) separately. Using the unique super-concentrated laser-induced thermal process, the laser printing method developed in this paper can integrate these processes into a one-step approach. This integrated fabrication technique can significantly economize energy, time, and auxiliary costs. Laser printing is a drop-on-demand process that can be easily integrated with automatic manufacturing systems. We have constructed an automatic laser printing system that combines the laser scribing machine with a robotic arm displacement system and demoed the automatic laser printing process. Supplementary Fig. S2a shows the entire setup of the automatic laser printing system. The robotic arm displaces the donor slide to different positions on the carbon fabric acceptor for laser printing and collects the scribed donor slide after printing. Supplementary Movie 1 shows the automatic laser printing process. Supplementary Movie 2 and Supplementary Fig. S2b and d present the microscope camera view of the laser printing process captured by the microscope camera in Supplementary Fig. S2a. It can be observed that laser-induced jetting is accompanied by intense plasma during the laser scribing process. Most precursor materials in the donor layer are activated and transferred onto the carbon fabric acceptor. After laser-scribing three donor slides at different positions on the carbon fabric acceptor, a laser-printed $6 \times 6\ cm^{-2}$ sample is obtained (as shown in Supplementary Fig. S2c). The printing process
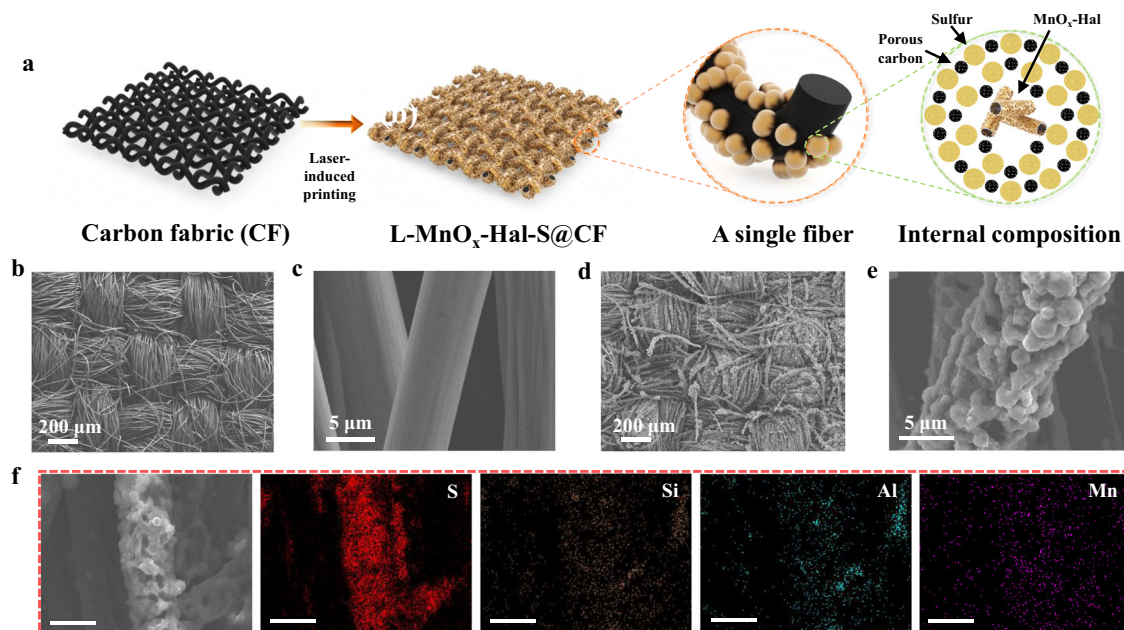
Fig. 2 | Conversion of carbon fabric into laser-printed cathode. a Illustration of the transformation from a bare carbon fabric to an L-MnO$_x$-Hal-S@CF cathode. The enlarged part shows that a single fiber includes a carbon fiber core (the black one) and a composite coating (the brown balls). The composite coating is composed of porous carbon, sulfur species, and MnO$_x$-Hal nanotubes. **b, c** SEM images of a bare carbon fabric. **d, e** SEM images of a L-MnO$_x$-Hal-S@CF cathode. **f** EDS mapping of the L-MnO$_x$-Hal-S@CF cathode (scale bar: 10 µm).

takes less than 20 min (including donor displacement time), significantly less than the time consumed by traditional manufacturing routes. Therefore, scalable and efficient sulfur cathode fabrication can be achieved through multiple laser printing aided by the automatic displacement system. In practical manufacturing, the laser and displacement system can be further integrated into an automatic production line, achieving large-scale production.

Characterization of laser-printed cathodes

As illustrated in Fig. 2a, after the laser printing process, a mixture containing host materials (MnO$_x$-Hal), active materials (sulfur), and conductive components (porous carbon) is printed onto the carbon fabric, forming a uniform integrated sulfur cathode (L-MnO$_x$-Hal-S@CF). The main components of the MnO$_x$-Hal coating are sulfur species. The MnO$_x$-Hal nanotubes serve as both host and structural materials supporting the sulfur species. The porous carbon species are mixed within the sulfur species. Scanning electron microscopy (SEM) images of the bare carbon fabric (Fig. 2b, c) and L-MnO$_x$-Hal-S@CF (Fig. 2d, e) demonstrate that uniform layers were coated onto the carbon fibers after the laser printing process. The energy-dispersive spectroscopy (EDS) mapping results (Fig. 2f) show an even distribution of S, Si, Al, and Mn in the cathode. The Si and Al correspond to the halloysite (Al$_2$O$_3$·2SiO$_2$·4H$_2$O), while the Mn corresponds to the manganese oxides. These results indicate that the sulfur-based mixture coating was successfully printed onto the carbon fabric.

To confirm that the manganese oxides were successfully synthesized on the halloysite nanotubes, the L-MnO$_x$-Hal-S@CF sample was treated with ultrasonic separation to obtain separated nanotube samples for transmission electron microscopy (TEM) analysis. Supplementary Fig. 3a shows the TEM images of a synthesized MnO$_x$-Hal nanotube. Inset of Fig. 3a illustrates the proposed model of a single MnO$_x$-Hal nanotube. Manganese oxide nanoparticles (the brown balls) are homogeneously distributed on the walls of the halloysite nanotube. Compared with the non-loaded halloysite nanotubes (Supplementary Fig. S3), the synthesized MnO$_x$-Hal nanotube exhibits a granular-structure surface. The high-resolution transmission electron microscopy (HRTEM) image (Fig. 3b) reveals that the distributed

particles are nanocrystals with sizes of ~ 5 nm. The lattice spacings of 0.21 nm and 0.24 nm respectively, correspond to the (111) and (101) planes of MnO$_2$[12,40]. In contrast, the non-loaded halloysite nanotube shows an almost non-crystalline structure (Supplementary Fig. S3c). The EDS mapping results (Fig. 3c) further indicate that Mn was uniformly distributed on the nanotube, confirming the uniform distribution of manganese oxide nanoparticles. Some Mn signals outside the nanotube sample relate to the manganese oxide nanoparticles in the surrounding porous carbon. Meanwhile, the sulfur signal corresponds to the chemically bonded sulfur. (Most of the physically bonded sulfur was separated from the L-MnO$_x$-Hal nanotube by ultrasonic treatment.) Therefore, these results demonstrate that the manganese oxide–doped halloysite nanotubes have been successfully synthesized in the one-step laser-printed process. For X-ray diffraction (XRD) and X-ray photoelectron spectroscopy (XPS) analysis, we scraped the L-MnO$_x$-Hal-S and L-Hal-S powders from the surfaces of L-MnO$_x$-Hal-S@CF and L-Hal-S@CF samples. The XRD results (Fig. 3d) show that the main components of the L-MnO$_x$-Hal-S samples are sulfur, manganese oxide, and halloysite[41]. The broad peak ($2\theta = $ ~ 26°) corresponds to the glucose-derived carbon. The Raman spectra (Supplementary Fig. S4) also show the successful transfer of the sulfur-based coating onto the carbon fabric. The nearly overlapping D and G peaks indicate the formation of hybrid carbon (derived from glucose). The XPS spectra of the L-MnO$_x$-Hal-S and L-Hal-S powders were investigated to confirm the elemental states of the samples. The XPS survey spectrum of L-MnO$_x$-Hal-S (Supplementary Fig. S5) reveals O, Mn, C, S, Si, and Al to be the major elements. The Mn 2p spectrum (Fig. 3e) indicates that the Mn atoms exhibit three chemical states, namely Mn^{2+}, Mn^{3+}, and Mn^{4+}, corresponding to different manganese oxides[42–44]. Therefore, the synthesized manganese oxide nanoparticles can be considered manganese oxide hybrids (MnO$_x$). The multiple chemical states of Mn atoms suggest that the generated manganese oxides have multiple crystal structures, likely due to the concentrated laser-induced thermal process. Multiple crystal structures form during the transient heating and cooling process. Variations in laser energy density may lead to different chemical states of the Mn atoms. The electrochemical performance of the cathodes can be regulated in this manner. However,
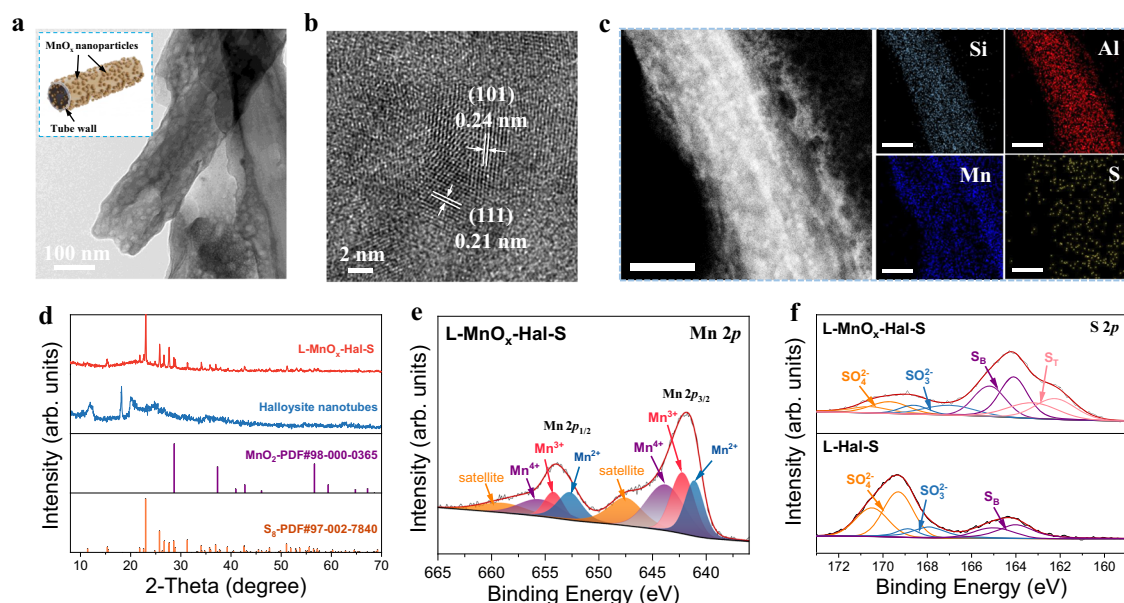
Fig. 3 | Characterizations of the L-MnO$_x$-Hal nanotube. a TEM image of a single L-MnO$_x$-Hal nanotube. Inset shows the illustration of a single L-MnO$_x$-Hal nanotube, which is composed of the halloysite nanotube and embedded MnO$_x$ nanoparticles (the brown balls). **b** HRTEM image of the L-MnO$_x$-Hal nanotube. The lattice spacings of 0.21 nm and 0.24 nm respectively, correspond to the (111) and (101) planes of MnO$_2$. **c** EDS mapping of the L-MnO$_x$-Hal nanotube (scale bar: 50 nm). **d** XRD spectra of the samples. **e** High-resolution Mn 2p XPS spectrum and (**f**) high-resolution S 2p spectra of the samples.

the pulse energy density significantly affects the laser printing processes. A laser pulse with low energy density may not activate the precursor layer, preventing the printing of precursor materials. Conversely, a laser pulse with high energy density could damage the glass substrate and result in the loss of precursor materials. Therefore, the range of pulse energy density suitable for laser printing is limited for a precursor sheet with a specific composition. The optimal pulse energy density range for the precursor sheet used in this work is approximately 7.8–10.9 J cm^{-2}. We fabricated three samples under pulse energy densities ranging from 7.8 to 10.9 J cm^{-2}. The detailed laser parameters are listed in Supplementary Table S1. Supplementary Fig. S6 shows the high-resolution Mn 2p spectra of the L-MnO$_x$-Hal-S samples fabricated under different pulse energy densities. With increasing pulse energy density, the samples show a small increase in high-valence Mn signals. However, because the increment in energy density is not substantial, the differentiation in the chemical states of Mn atoms is minimal. According to our earlier study, the electrochemical performances of the L-MnO$_x$-Hal-S@CF cathodes fabricated under pulse energy densities ranging from 7.8 to 10.9 J cm^{-2} are similar. The S 2p spectrum (Fig. 3f) indicates that the primary chemical states of sulfur atoms in L-MnO$_x$-Hal-S include terminal sulfur (S$_T$), bridge sulfur (S$_B$), SO$_3^{2-}$, and SO$_4^{2-}$. The S$_T$ bonds correspond to elemental sulfur (S$_8$), while the S$_B$ bonds indicate that partial sulfur atoms were bonded with the porous carbon and carbon fibers during laser printing. The SO$_3^{2-}$ and SO$_4^{2-}$ bonds suggest that partial sulfur atoms were bonded with halloysite or manganese oxides. These results demonstrate that the laser printing process not only transferred elemental sulfur but also activated the formation of polysulfides. In comparison, the ratio of the SO$_3^{2-}$ / SO$_4^{2-}$ bonds in L-Hal-S is higher than that in L-MnO$_x$-Hal-S. Meanwhile, the ratio of S$_B$ bonds is lower, and S$_T$ bonds are nearly absent. The higher ratio of high-valence sulfur in L-Hal-S indicates that the precursor materials of L-Hal-S absorbed more laser energy, resulting in greater oxidation of sulfur atoms. The decomposition of Mn(NO$_3$)$_2$ consumes part of the laser energy and accelerates the release of the precursor material, leading to a decrease in polysulfide generation. These high-valence polysulfides may contribute to a different LiPS conversion model in laser-printed cathodes compared with elemental sulfur cathodes.

The MnO$_x$-Hal nanotubes in the laser-printed L-MnO$_x$-Hal-S@CF cathode are expected to serve as efficient 3D sulfur hosts for mitigating the shuttle effect. Manganese oxides with various nanostructures have been widely employed as sulfur hosts in Li–S batteries[45,46]. In addition, halloysite nanotubes have been proven to be effective supporters in the synthesis of 3D sulfur hosts[26,47]. The introduction of halloysite nanotubes prevents the formation of bulky manganese oxides. As the laser-induced thermal process is concise, the generated manganese oxides exist in multiple crystal structures (as shown in the discussion of the XPS and TEM results). Therefore, it is hard to discuss the promotion mechanism of these MnO$_x$-Hal on the evolution of polysulfides at a molecular level. To demonstrate the role of MnO$_x$-Hal as a sulfur host, we individually fabricated the MnO$_x$-Hal nanotube sample using the same laser setting as that for the L-MnO$_x$-Hal-S@CF cathode. A polysulfide (Li$_2$S$_4$) adsorption test was conducted to compare the absorbability of carbon fabric, raw halloysite, and MnO$_x$-Hal on polysulfides. As shown in Supplementary Fig. S7, the MnO$_x$-Hal nanotube exhibit strong absorbability to lithium polysulfides. The Li$_2$S$_4$ solution became almost transparent after 2 hours of adsorption (Supplementary Fig. S7a). In contrast, carbon fabric and raw halloysite nanotubes show minimal absorbability. The UV-vis absorption spectra (Supplementary Fig. S7b) further demonstrate that Li$_2$S$_4$ was almost entirely absorbed by the MnO$_x$-Hal after 12 h. These results indicate that the fabricated MnO$_x$-Hal can efficiently absorb lithium polysulfides and attenuate the shuttle effect in the Li–S battery. The practical enhancement of MnO$_x$-Hal on the Li–S battery performance is demonstrated in Supplementary Fig. S8. Here, the traditional melting-diffusion process is used to encapsulate sulfur into the MnO$_x$-Hal and raw halloysite. They are then assembled into a conventional tape-casting cathode (with a sulfur mass of ~ 2.0 mg cm^{-2}) for measurement. The battery performance indicates that the fabricated MnO$_x$-Hal exhibits a significant improvement in initial capacity (1188 mAh g^{-1} at 0.2 C) and cycling stability (87.7% of the initial value at the 50th cycle). In contrast, the improvement of raw halloysite on battery performance is minimal, likely due to the strong absorbability of MnO$_x$-Hal to lithium polysulfides. MnO$_x$-Hal can reduce the shuttle effect in the Li–S battery. However, due to the low electrical conductivity of halloysite and manganese oxides, the electron transport of the MnO$_x$-Hal-based

sulfur cathode may be poor. In addition, halloysite itself shows little enhancement on Li−S battery performance. The halloysite nanotubes mainly act as structural materials in the cathodes. Therefore, a high ratio of halloysite nanotubes may lead to a decline in the total specific capacity of the cathode. Thus, the ratio of the MnO$_x$-Hal nanotubes used in the cathodes should be considered carefully.

It should be noted that halloysite nanotubes act as supporters during the synthesis of 3D host materials (MnO$_x$-Hal) and stabilizers during the laser printing process. In our preliminary experiments, we attempted to fabricate laser-printed sulfur cathodes using a donor containing only sulfur and glucose (donor preparation details given in the experimental section). The resulting sample is designated as S-C@CF. However, only ~10% of the sulfur was found to be transferred onto the carbon fabric acceptor. Supplementary Fig. S9 presents the SEM images of the laser-printed S-C@CF sample, revealing that the transferred materials on the carbon fibers are small and uneven. This result can be attributed to the low thermostability of sulfur. By adding halloysite nanotubes to the donor, the transfer rates of sulfur can be significantly improved. Consequently, the sulfur loadings in the laser-printed samples can be adjusted by tuning the sulfur loadings in the halloysite-sulfur-based donors. We fabricated different laser-printed L-MnO$_x$-Hal-S@CF samples using halloysite-sulfur-based donors with varying sulfur loadings (3, 6, and 9 mg cm^{-2}). The actual sulfur loadings in the samples were confirmed through thermogravimetric analysis (TGA). Based on the TGA data (as shown in Supplementary Fig. S10), the calculated results (listed in Supplementary Table S2) show that when using a donor with sulfur content of 3, 6, and 9 mg cm^{-2}, the laser-printed samples deliver sulfur loadings of 2.1, 4.6, and 7.8 mg cm^{-2}, respectively. This means that the transfer rates of sulfur are 70.7%, 76.6%, and 86.9%, respectively. The SEM images of L-MnO$_x$-Hal-S@CF samples with different sulfur loadings are shown in Supplementary Fig. S11. It can be observed that the halloysite-sulfur-based coatings on carbon fabrics gradually increase with increased sulfur loadings.

Battery performance of the Li−S cells

The detailed electrochemical performances of the L-MnO$_x$-Hal-S@CF cathodes were measured by assembling them into Li−S coin batteries. To determine the accelerated evolution kinetics of lithium polysulfides through the MnO$_x$-Hal host in the L-MnO$_x$-Hal-S@CF cathode, the L-Hal-S@CF cathode was fabricated as a control sample. The fabrication processes for the L-Hal-S@CF cathode are identical to those of L-MnO$_x$-Hal-S@CF, except for the addition of manganous nitrate to the donor. The sulfur loading in the L-Hal-S@CF cathode is approximately 2.0 mg cm^{-2}. The cyclic voltammetry (CV) curves (at 0.1 mV s^{-1}) are shown in Fig. 4a. For the L-MnO$_x$-Hal-S@CF cathode (with sulfur loading of ~2.1 mg cm^{-2}), the negative peak at ~2.32 V (peak A) indicates the reduction of S$_8$ to soluble long-chain polysulfides Li$_2$S$_n$ (4 ≤ n ≤ 8). The peak at ~2.05 V (peak B) further indicates the generation of insoluble short-chain Li$_2$S$_2$/Li$_2$S[22,48]. Meanwhile, the positive peak (peak C) at ~2.45 V can be attributed to the oxidization from Li$_2$S$_2$/Li$_2$S to Li$_2$S$_n$ and further S$_8$[16,49,50]. It should be noted that the L-Hal-S@CF and L-MnO$_x$-Hal-S@CF cathodes show different LiPS conversion models. Usually, the discharge processes of a typical Li−S battery include a first stage at a high voltage range (around 2.4–2.05 V) and a second stage at a low voltage range (around 2.05–1.5 V). These two stages correspond to the reduction of S$_8$ to long-chain polysulfides Li$_2$S$_n$ (4 ≤ n ≤ 8) and further to short-chain Li$_2$S$_2$/Li$_2$S, respectively. The first-stage reduction typically delivers a theoretical capacity of 418 mAh g^{-1}. However, for sulfur cathodes containing a high ratio of polysulfides, the evolution of LiPS may not adhere to the rule of two-step reduction because their reductions do not start from elemental sulfur. Some reports suggest that the discharge processes of poly-sulfide cathodes (e.g., S$_3^{2-}$, Li$_2$CS$_3$, sulfurized polyacrylonitrile, etc.) only include a single stage[51–54]. All the evolutions of LiPS are mixed in this stage, and the corresponding CV curves show a single discharge

peak. Consequently, the discharge capacities of these polysulfide cathodes between 2.4 and 2.05 V are higher than those of elemental sulfur cathodes (418 mAh g^{-1}) due to the complex multistep dissocia-tion processes. The high-resolution S 2p spectrum (Fig. 3f) indicates that the sulfur species in the L-Hal-S@CF cathode are mainly poly-sulfides. The L-Hal-S@CF cathode shows a single discharge peak in the CV curve and a single discharge stage in the charge-discharge curve. These performances are similar to those of reported polysulfide cathodes. Therefore, the L-Hal-S@CF cathode demonstrates a polysulfide-dominated charge-discharge mode. The high-valence sul-fur species in L-MnO$_x$-Hal-S are significantly fewer than those in L-Hal-S. These polysulfide species may also contribute to a polysulfide con-version mechanism. The high intensity of peak A and the broadening of peaks A and B in the rate test indicate that the laser-printed cathode may contain a polysulfide conversion mechanism[51,55]. Research on polysulfide cathodes suggests that the multistep dissociation pro-cesses of polysulfides contribute to higher cycling stability[53,55]. How-ever, some inactive polysulfides may not be able to participate in the LiPS conversion, which could explain why the L-Hal-S@CF cathode exhibits poorer specific capacity than the L-MnO$_x$-Hal-S@CF cathode.

To investigate the Li$^+$ diffusion properties within the L-MnO$_x$-Hal-S@CF and L-Hal-S@CF cathodes, CV curves were tested at sweep rates between 0.1 and 0.5 mV s^{-1} (Fig. 4b, c). According to the Randles−Sevcik equation[56–58], the diffusion coefficient of lithium ions (D$_{Li+}$) can be determined using the following formula:

$$I_p = a D_{Li+}^{0.5} v^{0.5}, \qquad (2)$$

where a is a constant related to the number of transferred electrons, the concentration of Li$^+$, and the electrode area, v is the sweep rate, and I_p is the peak current at different sweep rates. Therefore, D$_{Li+}$ can be determined through the slope of the fitted curves of I_p versus $v^{0.5}$. Figure 4d shows the I_p values versus $v^{0.5}$ and the fitted curves of peaks A and C in the two cathodes. The L-MnO$_x$-Hal-S@CF cathode exhibits higher slopes in both peaks A and C, indicating a higher Li$^+$ diffusion coefficient in the L-MnO$_x$-Hal-S@CF cathode during both charging and discharging. The galvanostatic charge-discharge results (0.2 C) are presented in Fig. 4e. Compared with the L-Hal-S@CF cathode, the L-MnO$_x$-Hal-S@CF cathode delivers a lower polarization potential, which aligns with the CV results. This result is attributed to the rapid evolution of polysulfide species accelerated by the MnO$_x$-Hal host. Supplementary Fig. S12 presents the electrochemical impedance spectroscopy (EIS) (Nyquist plots) for the L-MnO$_x$-Hal-S@CF and L-Hal-S@CF samples. The inset in Supplementary Fig. S12 shows the corresponding fitted equivalent circuit. The calculated impedance values are listed in Supplementary Table S3. Compared with the L-Hal-S@CF cathode, the L-MnO$_x$-Hal-S@CF cathode exhibits lower ohmic resistance (R$_s$), charge transport impedance (R$_{ct}$), and lithium-ion diffusion impedance (Z$_w$). This demonstrates that the manganese oxide particles significantly improve the ion and electron transmission efficiency of the halloysite-based cathode. The chemical adsorption and catalytic activity of MnO$_x$-Hal on LiPS are investigated through ex-situ Mn 2p XPS spectra of L-MnO$_x$-Hal-S in different charge/discharge states. The ex-situ XPS results (Fig. 4f) confirm that the MnO$_x$ nanoparticles can attract electrons from LiPS to form low-valence Mn bonds during the discharging process, thus enhancing the fast conversion of LiPS. The chemical states of the Mn atoms are restored after full charging. These results indicate that MnO$_x$-Hal exhibits intense catalytic activity on LiPS conversion[27]. We further investigated the EDS mapping of cycled L-MnO$_x$-Hal nanotube samples under TEM analysis (Supplementary Fig. S13). The EDS mapping shows that the sulfur signal in the cycled sample is significantly higher than in the initial sample (Fig. 3c). Meanwhile, the distribution of the S signal is similar to that of the Mn signal. Considering most of the physically bonded sulfur was separated from the L-MnO$_x$-Hal nanotube by
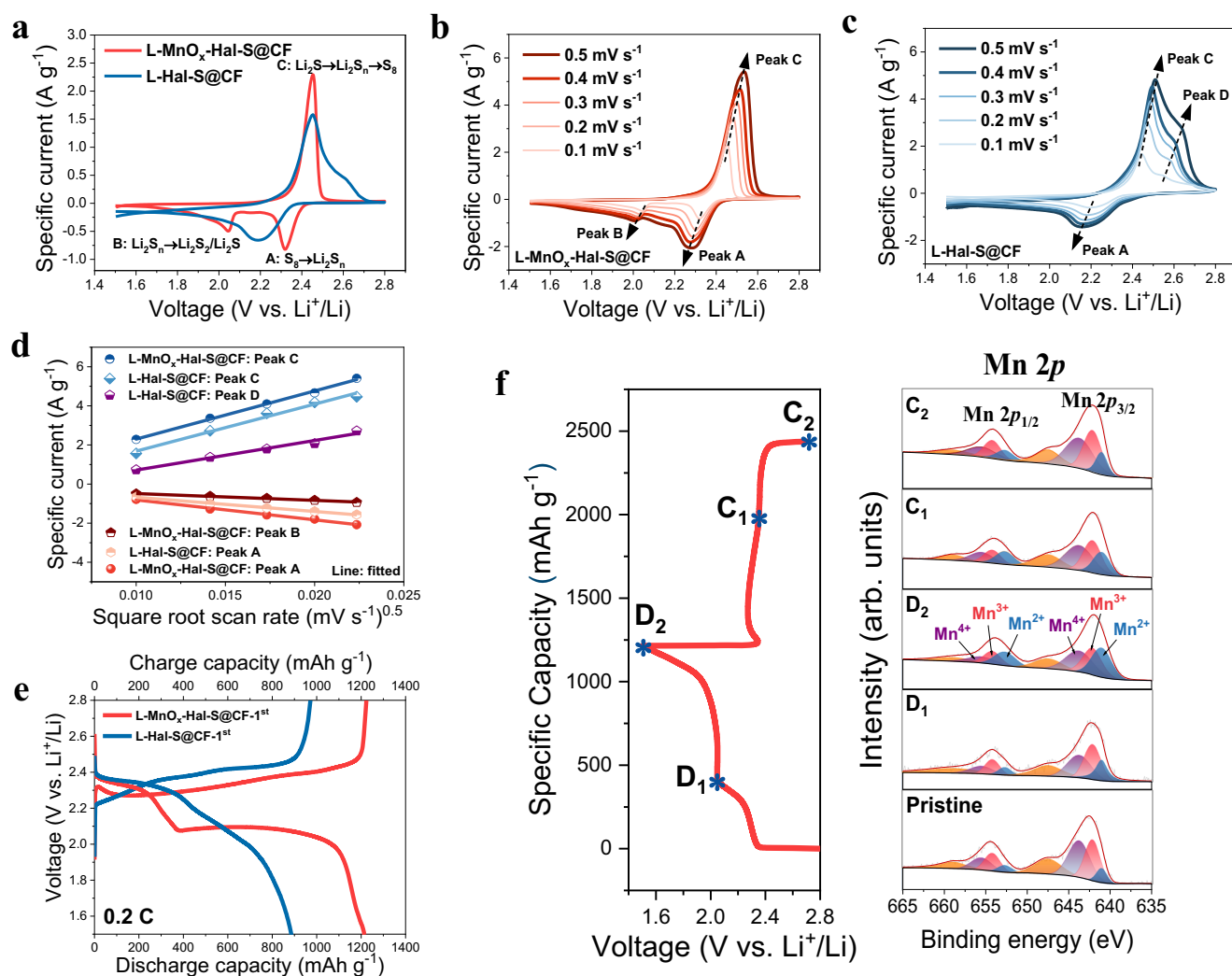
Fig. 4 | Electrochemical performances of the Li-S batteries. a CV curves at 0.1 mV s^{-1} for the L-MnO$_x$-Hal-S@CF and L-Hal-S@CF cathodes. CV curves for the (**b**) L-MnO$_x$-Hal-S@CF cathode and (**c**) L-Hal-S@CF cathode at different scan rates. **d** Fitted curves of peak current densities *vs* square root scan rates. **e** Charge-discharge curves at 0.2 C. **f** Ex situ Mn 2*p* spectra of L-MnO$_x$-Hal-S samples in different charge/discharge states. The five Mn 2*p* spectra in the right part (from the bottom to the top) correspond to the pristine state, first discharge state (D$_1$), second discharge state (D$_2$), first charge state (C$_1$), and second charge state (C$_2$), which are signed in the charge-discharge curve (the left part).

ultrasonic treatment (as discussed in Fig. 3c), these S signals could be attributed to the chemically bonded sulfur. The centrally distributed chemically bonded sulfur in the cycled sample and the ex-situ XPS results indicate that the MnO$_x$-Hal can effectively absorb the generated polysulfides during cycling. The characterization of morphology and surface chemical composition in cycled lithium anodes can also confirm the effectiveness of polysulfide-shuttling mitigation. Supplementary Fig. S14a and b show that the cycled lithium anode paired with the L-MnO$_x$-Hal-S@CF cathode exhibits smoother and denser lithium deposition than that paired with the L-Hal-S@CF cathode. The XPS results (Supplementary Fig. S14c and d) also indicate that the cycled lithium anode paired with the L-MnO$_x$-Hal-S@CF cathode is bonded with fewer polysulfides compared to that paired with the L-Hal-S@CF cathode. This suggests that L-MnO$_x$-Hal absorbs LiPS and mitigates parasitic reactions between LiPS and Li metal. These results indicate that L-MnO$_x$-Hal can effectively absorb LiPS and facilitate efficient LiPS reaction kinetics. Therefore, the shuttle effect can be mitigated, and the dead sulfides deposited on the lithium anode can be reduced (Fig. 5a).

Figure 5b illustrates the cycling performances of Li–S batteries (0.2 C) utilizing the L-MnO$_x$-Hal-S@CF and L-Hal-S@CF cathodes. The

L-MnO$_x$-Hal-S@CF cathode shows a significantly higher initial specific capacity of 1215 mAh g^{-1} compared with the L-Hal-S@CF cathode (886 mAh g^{-1}). The residual capacity of the L-MnO$_x$-Hal-S@CF cathode at the 200th cycle (993 mAh g^{-1}, 81.7% remained) is also higher than that of the L-Hal-S@CF cathode (581 mAh g^{-1}, 65.5% remained). The corresponding galvanostatic charge-discharge curves are presented in Supplementary Fig. S15. The charge and discharge potential platforms of the L-MnO$_x$-Hal-S@CF cathode remain almost the same during all 200 cycles, while the discharge potential platforms of the L-Hal-S@CF cathode gradually decline. The rate performances are depicted in Fig. 5c. As the current density increases from 0.2 to 5 C, the specific capacity of the L-MnO$_x$-Hal-S@CF cathode decreases to 492 mAh g^{-1}, which is significantly higher compared with the L-Hal-S@CF cathode (312 mAh g^{-1}). When the current density switches to 0.2 C, the specific capacity of the L-MnO$_x$-Hal-S@CF cathode resumes to 1051 mAh g^{-1} and maintains low decay over the subsequent ten cycles. In contrast, the specific capacity of the L-Hal-S@CF cathode only resumes to 769 mAh g^{-1} when the current density switches to 0.2 C, and it experiences a significant capacity decline during the subsequent ten cycles. Figure 5d and Supplementary Fig. S16 show the charge-discharge curves of both cathodes under varying current densities.
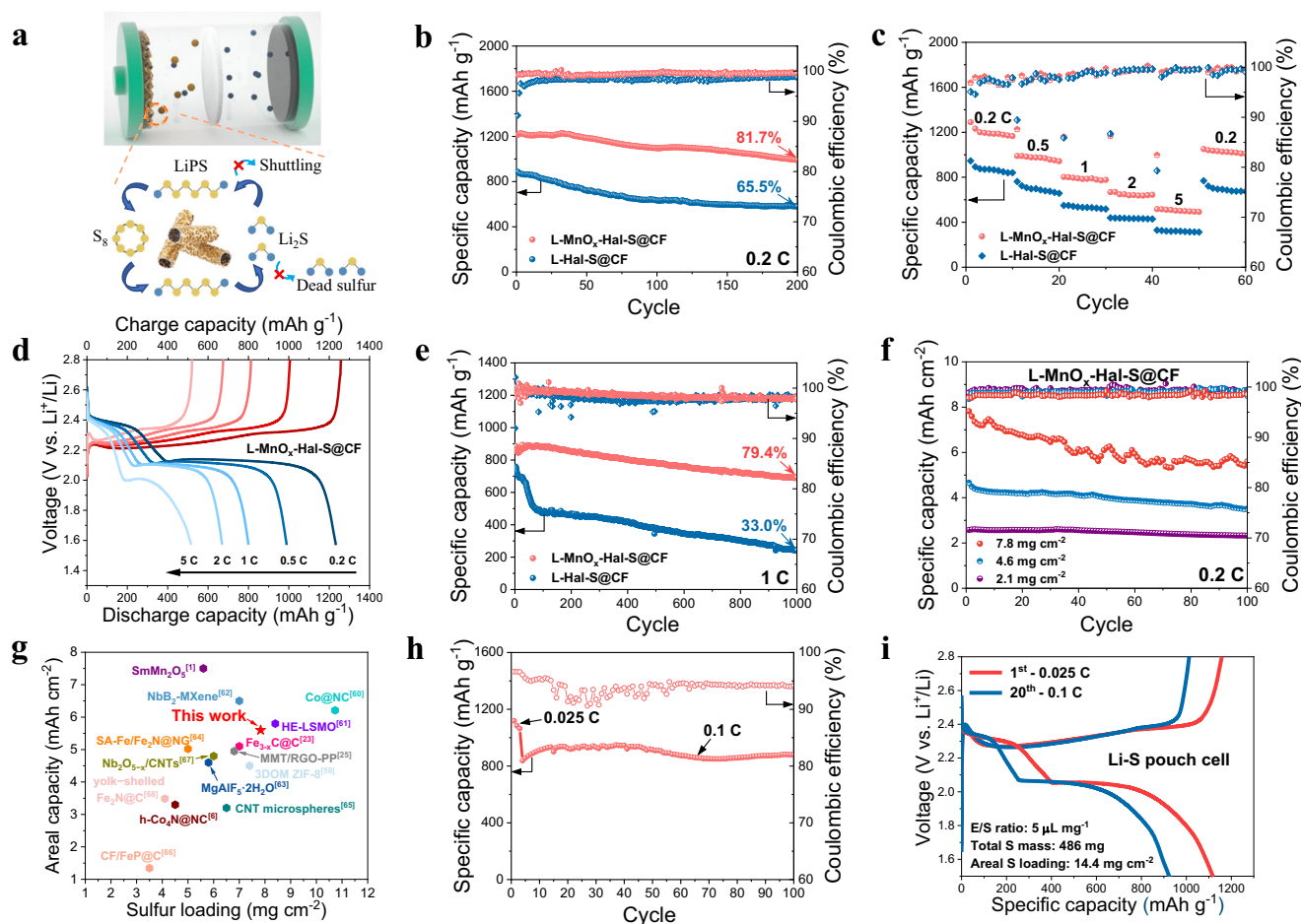
Fig. 5 | Cycling performances of the Li-S coin and pouch cells. a Illustration of L-MnOx-Hal-S@CF cathode stabilizing the lithium polysulfide (LiPS). **b** Cyclic performances at 0.2 C for the L-MnOx-Hal-S@CF and L-Hal-S@CF cathodes. **c** Rate performances for the L-MnOx-Hal-S@CF and L-Hal-S@CF cathodes. **d** Charge-discharge curves of the L-MnOx-Hal-S@CF cathode under different current densities. **e** Cyclic performances at 1 C for the L-MnOx-Hal-S@CF and L-Hal-S@CF cathodes. **f** Cyclic performances at 0.2 C for the L-MnOx-Hal-S@CF cathodes with different sulfur loadings. **g** Comparison of areal mass loading of sulfur and residual areal capacity between Li-S batteries based on reported sulfur cathodes and the L-MnOx-Hal-S@CF cathode. **h** Cyclic performance and (**i**) charge-discharge curves of the Li-S pouch cell.

The charge and discharge potential platforms of L-MnOx-Hal-S@CF remain almost stable as current densities increase. In contrast, for the L-Hal-S@CF cathode, the charge potential platforms gradually rise while the discharge potential platforms gradually decline with increasing current densities. The cyclic performances of the L-MnOx-Hal-S@CF and L-Hal-S@CF cathodes at 1 C are compared in Fig. 5e. With an initial specific capacity of 873 mAh g^{-1}, the L-MnOx-Hal-S@CF cathode retains 693 mAh g^{-1} (79.4% remained) after 1000 cycles at 1 C. In contrast, the L-Hal-S@CF cathode only presents an initial capacity of 735 mAh g^{-1} and a low residual capacity of 243 mAh g^{-1} (33.0% remained). The corresponding galvanostatic charge-discharge (GCD) curves (Supplementary Fig. S17) also indicate stable charge and discharge potential platforms during prolonged cycling at 1 C. The 0.2 C cyclic performances for L-MnOx-Hal-S@CF cathodes with varying sulfur mass loadings are given in Fig. 5f. As sulfur mass loadings increase from 2.1 to 7.8 mg cm^{-2}, the initial areal capacities of the L-MnOx-Hal-S@CF cathodes rise from 2.58 to 7.82 mAh cm^{-2}. In the 100th cycle, the L-MnOx-Hal-S@CF cathode with 7.8 mg cm^{-2} sulfur presented a remaining areal capacity of 5.60 mAh cm^{-2} (71.6 % remained). The capacity retention is close to that of low-sulfur-loading samples. The fabricated L-MnOx-Hal-S@CF cathode with high sulfur mass loading still demonstrates stable cyclic performance. In addition, the GCD curves (Supplementary Fig. S18) indicate that the L-MnOx-Hal-S@CF cathodes with different sulfur loadings maintain stable charge and

discharge potential platforms. To demonstrate the reproducibility of the laser-printed cathodes, we have fabricated multiple samples under the same settings. As shown in Supplementary Fig. S19, the different samples fabricated under the same settings deliver stable cyclic performances. The differences between different samples are slight. Compared with other reported sulfur cathodes, our L-MnOx-Hal-S@CF cathode also shows advantages in sulfur loading and residual areal capacity (Fig. 5g)[1,6,23,25,59–68]. The long-cyclic and rate performances of the L-MnOx-Hal-S@CF cathode could be attributed to the efficient MnOx-Hal sulfur host and the optimized porous cathode structure. Lithium polysulfide can be effectively anchored on the MnOx-Hal network during charging and quickly converted into soluble ions during discharging, contributing to a high retention rate of active polysulfide and, therefore, a small capacity decay. However, it is important to note that the battery performances of the L-MnOx-Hal-S@CF cathode are not at the highest level compared with some well-designed cathodes. There are certain drawbacks and limitations associated with the laser-printed cathodes. For instance, controlling the formation of host materials during the laser process is challenging due to the short and concentrated thermal processes generated by laser irradiation. Therefore, the fabricated host materials may consist of complex crystal structures. Sulfur cathodes using these hybrid host materials may exhibit lower performance than those using well-designed host materials. Additionally, the high transient temperature

can lead to the formation of polysulfides. Some of these may not convert into active sulfur species, resulting in decreased total capacity in the cathode. Nevertheless, the overall performance of the laser-printed cathodes remains satisfactory for practical applications. Supplementary Fig. S20 shows the microstructure of the L-MnOx-Hal-S@CF cathode (with a sulfur mass loading of 2.1 mg cm⁻²) after 1000-cycle charging-discharging at 1 C. The cathode's microstructure remains nearly unchanged. EDS mapping results further indicate that most sulfur species can be redeposited onto their original locations in the cathode. Meanwhile, the uniformly distributed Mn, Si, and Al suggest that the MnOx-Hal nanotubes remain stable after the cycling test. These results demonstrate that the L-MnOx-Hal-S@CF cathode exhibits high structural stability during cycling. Gravimetric and volumetric energy densities are critical metrics for assessing the practicability of a sulfur cathode. The energy densities of the L-MnOx-Hal-S@CF cathodes with varying sulfur loading were calculated when considering all battery components. The detailed calculation process is presented in Supporting Information. As shown in Supplementary Table S4, the gravimetric energy densities of the L-MnOx-Hal-S@CF-based batteries are 242, 381, and 549 Wh kg⁻¹, corresponding to sulfur loadings of 2.1, 4.6, and 7.8 mg cm⁻² respectively. Meanwhile, the volumetric energy densities are 122, 204, and 320 Wh L⁻¹ respectively. Due to the non-negligible density (12.4 mg cm⁻²) and thickness (290 μm) of the carbon fabric current collector, these values are slightly lower than those of traditional tape-casting cathodes using metal foil current collectors. However, the use of a porous carbon fabric current collector enhances ion migration and electron transfer during charging and discharging, ensuring high performance in high-loading sulfur cathodes. In addition, the flexibility of carbon-fabric-based cathodes contributes to their structural stability when assembled in a pouch cell. Using this kind of low-density porous current collector results in an inevitable trade-off, like in those reported high-sulfur-loading cathodes using porous current collectors, such as nickel foam[69], carbon nanotube (CNT) aerogel[70], and graphene sponge[71]. We further assembled a Li−S pouch cell using a double-side laser-printed L-MnOx-Hal-S@CF cathode. As shown in Fig. 5h, the assembled Li−S pouch cell delivers a high specific capacity of 1118 mAh g⁻¹ at 0.025 C with a high sulfur loading of 486 mg and a low electrolyte/sulfur (E/S) ratio of 5 μL mg⁻¹. When the current density becomes 0.1 C, the sulfur cathode undergoes an activation process (often observed in the literature[60,65,66]), reaching a high specific capacity of 948 mAh g⁻¹ at the 37th cycle. The remaining capacity is 880 mAh g⁻¹ at the 100th cycle, and the coulombic efficiency gradually stabilizes at 94%. We present a small screen displaying the characters "HKUST" illuminated by the Li−S pouch cell (as shown in Supplementary Fig. S21). The corresponding charge-discharge curves are consistent with the coin cell performance (Fig. 5i).

In summary, we have developed a single-step laser printing process for fabricating integrated sulfur cathodes for Li−S batteries. This method integrates sulfur host synthesis, sulfur encapsulation, and cathode fabrication into a one-step approach. The fabrication is time-saving and efficient. We fabricated a high-performance L-MnOx-Hal-S@CF cathode containing uniformly distributed sulfur, sulfur host materials, and a porous current collector. The assembled Li−S battery delivers high initial capacities and cyclic stability. The cathode loaded with over 7.8 mg cm⁻² sulfur demonstrates satisfactory areal capacity. Therefore, this research presents a promising method for efficiently preparing high-loading and high-performance sulfur cathodes, promoting the development of future commercial Li−S batteries. Despite these advantages, this technique has some drawbacks. For example, the fabricated host materials have complex crystal structures due to the short and concentrated laser-induced thermal processes. The high transient temperature can lead to the formation of polysulfides. Some of these may remain inactive, leading to a decrease in the total capacity of the cathode. Nevertheless, the overall performance of the laser-printed cathodes remains

satisfactory for practical applications. This fabrication strategy may inspire other battery research and open new research avenues.

Methods

Materials

All the starting materials used in this paper are commercially available. Halloysite nanotube (Al₂O₃·2SiO₂·4H₂O, Shanghai Aladdin) was used after washing and acid treatment. Chemicals include hydrochloric acid (HCl, Shanghai Aladdin, 37%), manganous nitrate (Mn(NO₃)₂·xH₂O, Shanghai Aladdin, 99.9%), dimethylsulfoxide (DMSO, Shanghai Aladdin, 99.8%), sodium dodecyl sulfate (SDS, Xilong Scientific, 98.5%), sublimed sulfur (Shanghai Aladdin, 99.5%), glucose (Thermo Fisher Scientific, 99.5%), poly(vinylidene fluoride) (PVDF, Arkema, 99.5%), N-Methyl-2-pyrrolidone (NMP, Shanghai Aladdin, 99%), lithium sulfide (Li₂S, Alfa Aesar, 99.5%), 1,2-dimethoxyethane (DME, Alfa Aesar, 99.5%), and 1,3-dioxolane (DOL, Alfa Aesar, 99.5%) were utilized directly. Carbon fabric (Cetech, thickness of 290 μm) was used as the acceptor in the laser printing process and current collector of the laser-printed cathode. Aluminum foil (Shenzhen Kejing, 99%, thickness of 20 μm) was used as the current collector of the tape-casting cathode. Lithium foil (Shenzhen Kejing, 99%, thickness of 150 μm) was used as an anode (negative electrode) in coin and pouch cells. Acetylene black (Shenzhen Kejing) was used as a conductive additive in tape-casting cathodes. Acetylene black (Shenzhen Kejing) was used as a conductive additive in tape-casting cathode. Celgard 2325 (Celgard, polypropylene/polyethylene/polypropylene three-layer structure, thickness of 25 μm, porosity of 40%, pore size of 0.03 μm) and polyethylene membrane (Celgard, thickness of 16 μm, porosity of 40%, pore size of 0.03 μm) were used as separators in coin and pouch cells, respectively. Electrolyte containing 1.0 M bis(trifluoromethanesulfonyl) imide (LiTFSI) and 1.0 wt.% lithium nitrate (LiNO₃) in a mixed solvent of DME and DOL (1:1 in volume) (Guangdong Canrd) was used in coin and pouch cells.

Pre-treatment of halloysite. The raw halloysite was washed several times using deionized (DI) water. Subsequently, 10 g of washed halloysite was added to 100 mL of 2 M HCl solution for water-bath heat treatment at 80 °C for 3 h. The treated mixture was washed several times until neutral and dried at 80 °C for 12 h to obtain well-separated halloysite nanotubes.

Preparation of precursor donor. First, 0.05 g of pre-treated halloysite nanotubes and 0.1 g of Mn(NO₃)₂·xH₂O were mixed and dispersed in 20 mL of DMSO under constant stirring at 80 °C for 2 h. Then, 0.05 g of glucose, 0.8 g of sulfur, and 1 mg of SDS were added to the mixture under constant stirring at 80 °C for another 2 h. Thereafter, a certain amount of the slurry mixture, ranging from 0.3 to 0.9 mL, was evenly coated onto a 2 × 2 cm² glass slide (corresponding to the sulfur loadings of 3 to 9 mg cm⁻² in donors). After drying at 60 °C for 5 h in an Ar-filled glovebox (H₂O < 0.1 ppm, O₂ < 0.1 ppm), the obtained slide was used as a precursor donor for the laser printing process. Precursor donors for fabricating control samples were also prepared through this method. For fabricating the S-C@CF sample, the corresponding donor was prepared with only sulfur, glucose, and SDS, while for the L-Hal-S@CF sample, the corresponding donor was prepared with only halloysite nanotubes, sulfur, glucose, and SDS. For the fabrication of the MnOx-Hal sample, the corresponding donor was prepared with only halloysite nanotubes and Mn(NO₃)₂·4H₂O. The content of other materials and the preparation process remain the same.

Laser printing process. A typical laser-induced printing process was employed to fabricate the hierarchical porous sulfur cathodes (positive electrodes). This process was conducted in an Ar-filled glovebox (H₂O < 0.1 ppm, O₂ < 0.1 ppm). The prepared precursor donor was placed above a bare carbon fabric acceptor, with a gap of 1 mm between them. The pulse laser was generated by a 1064 nm laser

engraving machine (MOPAB3, Diaoto). The detailed laser settings included a laser frequency of 100 kHz, a laser power of 4.65 W (measured by a power meter), a pulse width of 100 ns, and a scanning speed of 400 mm s^{-1}. After laser irradiation, a large amount of brown powder was coated onto the carbon fabric acceptor. The synthesized sample is designated as L-MnO$_x$-Hal-S@CF. The control samples S-C@CF and L-Hal-S@CF were fabricated using the same method. The sulfur mass loadings of the laser-printed cathodes depend on the content of the precursor and laser process. The corresponding values are listed in Supplementary Table S2. The MnO$_x$-Hal sample was fabricated using a similar approach with the same laser settings but with a glass slide acceptor. The fabricated brown MnO$_x$-Hal powder was collected from the glass slide for further analysis.

Preparation of tape-casting cathode. A typical melt diffusion method was utilized to synthesize the Hal/S and MnO$_x$-Hal/S composites. The raw halloysite and the fabricated MnO$_x$-Hal powders were evenly mixed with sulfur powder in a mass ratio of 1:4, respectively. The mixture was heated at a constant temperature of 155 °C for 12 h and then at 300 °C for 0.5 h under an argon atmosphere. After grinding, the obtained Hal/S and MnO$_x$-Hal/S powders were uniformly mixed with acetylene black and poly(vinylidene fluoride) (8:1:1 by weight) in NMP. The resulting slurry was evenly coated onto aluminum foil using a doctor blade with a gap of 100 μm. After drying at 50 °C for 12 h, the Hal/S and MnO$_x$-Hal/S cathodes were obtained with an areal sulfur loading of about 2.0 mg cm^{-2}.

Materials characterization. Scanning electron microscopy (JEOL-7800F) and transmission electron microscopy (JEOL-2010F) were employed to characterize the microstructure and morphology of the samples. Energy-dispersive spectroscopy (EDS, Oxford) was used to investigate the elemental distribution in the samples. XRD (PANalytical) was utilized to analyze the crystal structures of the samples from 5° to 90°. The molecular structure information of the samples was confirmed by Raman analysis (Micro-Raman, InVia, Renishaw). Thermogravimetric analysis (TGA, Q1000, TA) was conducted to confirm the sulfur loadings in the samples. XPS (Kratos Axis Ultra DLD) was used to investigate the chemical states of samples. In terms of the measurements of the unassembled electrode samples, they were cut into a suitable size and fixed on the sample holders in the Ar-filled glovebox. Then, the sample holders were sealed in an Ar-filled glass box and transported to the measurement equipment for testing. In terms of the ex-situ measurements of the assembled electrode samples (during charge/discharge states or after cycling), they were collected from the disassembled cells in the Ar-filled glovebox and washed in DME solution several times. After drying in the Ar-filled glovebox at 25 °C, they were sampled and transported to the measurement equipment using the same procedures as those for unassembled electrodes samples.

Adsorption tests for lithium polysulfide. The Li$_2$S$_4$ solution was prepared in an Ar-filled glovebox by mixing sulfur powder and Li$_2$S in a molar ratio of 3:1 in a mixed solvent of DME and DOL (1:1 in volume). The mixed solution was stirred at 50 °C overnight. Then, 10 mg of carbon fabric, halloysite powder, and MnO$_x$-Hal powder were separately dispersed into 10 mL of 0.2 mM Li$_2$S$_4$ solution. The visual concentration changes of the Li$_2$S$_4$ solution were recorded with a digital camera at different adsorption times. After 12 h of absorption, the ultraviolet-visible absorption spectra of these solutions were measured using a UV-vis spectrophotometer (Lambda 1050 +, PerkinElmer).

Electrochemical evaluation of the Li–S coin cells. The fabricated cathodes (positive electrodes), lithium anodes (negative electrodes), and separators were respectively cut into discs with a certain diameter using a punching machine (Shenzhen Kejing). The 2032-type coin cells

were assembled in an Ar-filled glovebox (H$_2$O < 0.1 ppm, O$_2$ < 0.1 ppm) using fabricated cathodes with a diameter of 12 mm, pure lithium foils with a diameter of 14 mm as counter/reference electrodes, Celgard 2325 with a diameter of 19 mm as separators, and Li–S battery electrolyte containing 1.0 M LiTFSI and 1.0 wt.% LiNO$_3$ in a mixed solvent of DME and DOL (1:1 in volume). Standard 2032-type stainless-steel coin cell case and a stainless-steel spring were used in these coin cells. The used electrolyte was purchased from the commercial corporation and stored in a sealed aluminum bottle inside the Ar-filled glovebox. A pipette with a polypropylene tip was used to transfer the electrolyte. The volume of the electrolyte used depended on the mass loading of sulfur in the cathode. The actual electrolyte/sulfur ratio (E/S ratio) and theoretical negative/positive capacity ratio (N/P ratio) are calculated and presented in Supplementary Table S4. Electrochemical impedance spectroscopy (EIS) tests (frequency: 10^5 to 10^{-2} Hz, amplitude: 10 mV) and cyclic voltammetry (CV) measurements (1.5–2.8 V vs. Li$^+$/Li) were performed using an electrochemical workstation (PARSTAT, 3000A-DX). The impedance curves were fit with the ZView software. Galvanostatic charge-discharge (GCD) tests (1.5–2.8 V vs. Li$^+$/Li) were conducted at various rates on a battery testing system (LAND, CT3002A). All electrochemical tests were performed at 25 °C without an environmental chamber and external pressure. The specific current and specific capacity values are calculated based on the mass of sulfur in cathodes (positive electrodes). The areal capacity values are calculated based on the geometric area of the cathodes.

Assembly and evaluation of the Li–S pouch cell. For the assembly of the Li–S pouch cell, an L-MnO$_x$-Hal-S@CF cathode with double-side sulfur loading was prepared through double-side laser printing. The average areal sulfur loading on each side was 7.2 mg cm^{-2}. The prepared L-MnO$_x$-Hal-S@CF cathode was cut into a square measuring 45 × 80 mm^2, including an active region of 45 × 75 mm^2 and a blank region of 45 × 5 mm^2 (used for connecting the cathode tab). Metallic lithium sheets were also cut to the same size. After connecting with the cathode and anode tabs, two Li anodes and one sulfur cathode were stacked layer by layer with polyethylene separators. Then, they were sealed in an aluminum foil bag in a dry room with a dew point below − 40 °C. The electrolyte used was the same as that in the Li–S coin cell evaluation. The E/S ratio was set as 5 μL mg^{-1}. The cyclic test of the Li–S pouch cell was conducted on a LAND battery testing system. The Li–S pouch cell was initially charged and discharged at 0.025 C for 3 cycles and subsequently tested at 0.1 C. All electrochemical tests were performed at 25 °C without an environmental chamber and external pressure. The specific capacity values are calculated based on the mass of sulfur in cathodes.

Data availability
All the data needed to evaluate the conclusions in the paper are presented in the paper, Supplementary Information, and Source Data file. Source data are provided in this paper.

References

1. Wang, L. et al. Design rules of a sulfur redox electrocatalyst for lithium–sulfur batteries. *Adv. Mater.* **34**, 2110279 (2022).
2. Chen, W. J. et al. Electrolyte regulation towards stable Lithium-Metal anodes in lithium–sulfur batteries with sulfurized polyacrylonitrile cathodes. *Angew. Chem. Int. Ed.* **59**, 10732–10745 (2020).
3. Zhao, M., Chen, X., Li, X. Y., Li, B. Q. & Huang, J. Q. An organodiselenide comediator to facilitate sulfur redox kinetics in lithium–sulfur batteries. *Adv. Mater.* **33**, 2007298 (2021).
4. Liu, F. et al. Dual redox mediators accelerate the electrochemical kinetics of lithium-sulfur batteries. *Nat. Commun.* **11**, 5215 (2020).
5. Wei, J. Y. et al. Shielding polysulfide intermediates by an organosulfur-containing solid electrolyte interphase on the Lithium anode in lithium–sulfur batteries. *Adv. Mater.* **32**, 2003012 (2020).

6. Sun, Z. et al. Catalytic polysulfide conversion and physiochemical confinement for lithium–sulfur batteries. *Adv. Energy Mater.* **10**, 1904010 (2020).

7. Wang, J. et al. Suppressing the shuttle effect and dendrite growth in Lithium-Sulfur batteries. *ACS Nano* **14**, 9819–9831 (2020).

8. Chen, Z. X. et al. Cathode kinetics evaluation in lean-electrolyte Lithium-Sulfur batteries. *J. Am. Chem. Soc.* **145**, 16449–16457 (2023).

9. He, S. et al. Asymmetric N-coordinated iron single-atom catalysts supported on graphitic carbon for polysulfide conversion in lithium-sulfur batteries. *Chem. Eng. J.* **454**, 140202 (2023).

10. Zhao, M., Peng, H. J., Li, B. Q. & Huang, J. Q. Kinetic promoters for sulfur cathodes in Lithium-Sulfur batteries. *Acc. Chem. Res.* **57**, 545–557 (2023).

11. Liu, Y. et al. An organodiselenide comediator to facilitate sulfur redox kinetics in lithium–sulfur batteries with encapsulating lithium polysulfide electrolyte. *Angew. Chem. Int. Ed. Engl.* **62**, https://doi.org/10.1002/anie.202303363 (2023).

12. Zhao, X., Wang, G. & Wang, H. Synthesis of free-standing MnO_2/reduced graphene oxide membranes and electrochemical investigation of their performances as anode materials for half and full lithium-ion batteries. *J. Nanoparticle Res.* **18**, 304 (2016).

13. Wang, S. et al. Mesoporous β-MnO_2/sulfur composite as cathode material for Li-S batteries. *Electrochim. Acta* **106**, 307–311 (2013).

14. Sun, Z. et al. Conductive porous vanadium nitride/graphene composite as chemical anchor of polysulfides for lithium-sulfur batteries. *Nat. Commun.* **8**, 14627 (2017).

15. Gu, X. et al. Ball-milling synthesis of ZnO@sulphur/carbon nanotubes and $Ni(OH)_2$@sulphur/carbon nanotubes composites for high-performance lithium-sulphur batteries. *Electrochim. Acta* **196**, 369–376 (2016).

16. Yang, D. et al. ZnSe/N-doped carbon nanoreactor with multiple adsorption sites for stable lithium-sulfur batteries. *ACS Nano* **14**, 15492–15504 (2020).

17. Balach, J., Jaumann, T. & Giebeler, L. Nanosized Li_2S-based cathodes derived from MoS_2 for high-energy density Li–S cells and Si–Li_2S full cells in carbonate-based electrolyte. *Energy Storage Mater.* **8**, 209–216 (2017).

18. Wang, S. et al. Insight into MoS_2–MoN heterostructure to accelerate polysulfide conversion toward high-energy-density lithium–sulfur batteries. *Adv. Energy Mater.* **11**, 2003314 (2021).

19. Liu, W. et al. Cobalt-doping of molybdenum disulfide for enhanced catalytic polysulfide conversion in Lithium-Sulfur batteries. *ACS Nano* **15**, 7491–7499 (2021).

20. Liu, Y. T. et al. $NiCo_2O_4$ Nanofibers as carbon-free sulfur immobilizer to fabricate sulfur-based composite with high volumetric capacity for lithium–sulfur battery. *Adv. Energy Mater.* **9**, 1803477 (2019).

21. Jiao, L. et al. Capture and catalytic conversion of polysulfides by in situ built TiO_2-MXene heterostructures for lithium–sulfur batteries. *Adv. Energy Mater.* **9**, 1900219 (2019).

22. Wang, H. et al. Construction of ultrathin layered MXene-TiN heterostructure enabling favorable catalytic ability for high-areal-capacity lithium–sulfur batteries. *Nano Micro Lett.* **14**, 189 (2022).

23. Zhang, Y. et al. Hierarchical defective Fe_{3-x}C@C hollow microsphere enables fast and long-lasting lithium–sulfur batteries. *Adv. Funct. Mater.* **30**, 2001165 (2020).

24. Xin, S. et al. Coupling of oxygen vacancies and heterostructure on Fe_3O_4 via an anion doping strategy to boost catalytic activity for Lithium-Sulfur batteries. *Small* **19**, 2207924 (2023).

25. Long, X. et al. Two-dimensional montmorillonite-based heterostructure for high-rate and long-life lithium-sulfur batteries. *Energy Storage Mater.* **52**, 120–129 (2022).

26. Zhang, Q. et al. Manipulating the conversion kinetics of polysulfides by engineering oxygen p-band of halloysite for improved Li-S batteries. *Small* **18**, 2105661 (2022).

27. Wang, T. et al. Strategies toward high-loading Lithium-Sulfur batteries. *ACS Energy Lett.* **8**, 116–150 (2023).

28. Fan, L. et al. Interlayer material selection for Lithium-Sulfur batteries. *Joule* **3**, 361–386 (2019).

29. Zhou, L. et al. Sulfur reduction reaction in lithium–sulfur batteries: Mechanisms, catalysts, and characterization. *Adv. Energy Mater.* **12**, 2202094 (2022).

30. Li, L. et al. Rational design of a well-aligned metal–organic framework nanopillar array for superior lithium-sulfur batteries. *Chem. Eng. J.* **454**, 140043 (2023).

31. Zhang, H., Zhang, C., Wang, H. & Liu, F. Ablation behavior of SiC_p/AA2024 composites irradiated by a single-pulse nanosecond laser. *Opt. Laser Technol.* **126**, 106075 (2020).

32. Jeon, J. W. et al. The effect of laser pulse widths on laser-Ag nanoparticle interaction: Femto- to nanosecond lasers. *Appl. Sci.* **8**, 112 (2018).

33. Hendow, S. T. & Shakir, S. A. Structuring materials with nanosecond laser pulses. *Opt. Express* **18**, 10188 (2010).

34. Huang, Y. et al. High-throughput automatic laser printing strategy toward cost-effective portable integrated urea tele-monitoring system. *Small Methods* **8**, 2301184 (2023).

35. Lee, C. K. W., Pan, Y., Yang, R., Kim, M. & Li, M. G. Laser-induced transfer of functional materials. *Top. Curr. Chem.* **381**, 18 (2023).

36. Yan, B. et al. Highly efficient and highly selective CO_2 reduction to CO driven by laser. *Joule* **6**, 2735–2744 (2022).

37. Yuan, Y. et al. Ultrafast shaped laser induced synthesis of MXene quantum dots/graphene for transparent supercapacitors. *Adv. Mater.* **34**, 2110013 (2022).

38. Ma, L. et al. One-step ultrafast laser induced synthesis of strongly coupled 1T-2H MoS_2/N-rGO quantum-dot heterostructures for enhanced hydrogen evolution. *Chem. Eng. J.* **445**, 136618 (2022).

39. Yi, W., Jiang, H. & Cheng, G. J. Mesoporous LDH metastructure from multiscale assembly of defective nanodomains by laser shock for oxygen evolution reaction. *Small* **18**, 2202403 (2022).

40. Zhao, Y. et al. Uncovering sulfur doping effect in MnO_2 nanosheets as an efficient cathode for aqueous zinc ion battery. *Energy Storage Mater.* **47**, 424–433 (2022).

41. Wang, J. et al. The role of MnO_2 crystal morphological scale and crystal structure in selective catalytic degradation of azo dye. *Environ. Sci. Pollut. Res.* **30**, 15377–15391 (2023).

42. Yan, G. et al. Phase and morphology transformation of MnO_2 induced by ionic liquids toward efficient water oxidation. *ACS Catal.* **8**, 10137–10147 (2018).

43. Shin, D. et al. Sol-gel-driven combustion wave for scalable transformation of $Mn(NO_3)_2$ precursors into MnO_{2-x}/MWCNT supercapacitor electrodes capable of electrochemical activation. *Carbon* **152**, 746–754 (2019).

44. Gao, F. et al. In-situ DRIFTS for the mechanistic studies of NO oxidation over α-MnO_2, β-MnO_2 and γ-MnO_2 catalysts. *Chem. Eng. J.* **322**, 525–537 (2017).

45. Liang, X. et al. A highly efficient polysulfide mediator for lithium-sulfur batteries. *Nat. Commun.* **6**, 5682 (2015).

46. Liu, Y. T., Liu, S., Li, G. R., Yan, T. Y. & Gao, X. P. High volumetric energy density sulfur cathode with heavy and catalytic metal oxide host for lithium–sulfur battery. *Adv. Sci.* **7**, 1903693 (2020).

47. Lin, Y., Wang, X., Liu, J. & Miller, J. D. Natural halloysite nano-clay electrolyte for advanced all-solid-state lithium-sulfur batteries. *Nano Energy* **31**, 478–485 (2017).

48. Castillo, J. et al. High energy density Lithium-Sulfur batteries based on carbonaceous two-dimensional additive cathodes. *ACS Appl. Energy Mater.* **6**, 3579–3589 (2023).

49. Qian, J. et al. Enhanced electrochemical kinetics with highly dispersed conductive and electrocatalytic mediators for lithium–sulfur batteries. *Adv. Mater.* **33**, 2100810 (2021).

50. Li, Y. et al. Cobalt single atoms supported on N-doped carbon as an active and resilient sulfur host for lithium–sulfur batteries. *Energy Storage Mater.* **28**, 196–204 (2020).

51. Zhang, X. et al. Structure-related electrochemical behavior of sulfur-rich polymer cathode with solid-solid conversion in lithium-sulfur batteries. *Energy Storage Mater.* **45**, 1144–1152 (2022).

52. Cuisinier, M., Hart, C., Balasubramanian, M., Garsuch, A. & Nazar, L. F. Radical or Not Radical: Revisiting Lithium-Sulfur Electrochemistry in Nonaqueous Electrolytes. *Adv. Energy Mater.* **5**, 1401801 (2015).

53. Li, N. et al. An aqueous dissolved polysulfide cathode for lithium-sulfur batteries. *Energy Environ. Sci.* **7**, 3307–3312 (2014).

54. Zhang, X. et al. Structure-related electrochemical performance of organosulfur compounds for lithium-sulfur batteries. *Energy Environ. Sci.* **13**, 1076–1095 (2020).

55. Sul, H., Bhargav, A. & Manthiram, A. Lithium trithiocarbonate as a dual-function electrode material for high-performance lithium–sulfur batteries. *Adv. Energy Mater.* **12**, 2200680 (2022).

56. Shi, K. et al. Achieving balanced behavior between polysulfides adsorption and catalytic conversion from heterostructure Fe_3C-Fe_3P promotor for high-performance lithium-sulfur batteries. *Chem. Eng. J.* **460**, 141794 (2023).

57. Wang, H. et al. Reversible cross-linked phosphorylate binder for recyclable lithium-sulfur batteries. *Chem. Eng. J.* **452**, 139128 (2023).

58. Xie, Y. et al. MOF-Derived bifunctional $Co_{0.85}Se$ nanoparticles embedded in N-doped carbon nanosheet arrays as efficient sulfur hosts for Lithium-Sulfur batteries. *Nano Lett* **21**, 8579–8586 (2021).

59. Cui, G. et al. Three-dimensionally ordered macro-microporous metal organic frameworks with strong sulfur immobilization and catalyzation for high-performance lithium-sulfur batteries. *Nano Energy* **72**, 104685 (2020).

60. Li, Y. et al. Manipulating redox kinetics of sulfur species using mott-Schottky electrocatalysts for advanced Lithium-Sulfur batteries. *Nano Lett.* **21**, 6656–6663 (2021).

61. Tian, L., Zhang, Z., Liu, S., Li, G. & Gao, X. High-entropy perovskite oxide nanofibers as efficient bidirectional electrocatalyst of liquid-solid conversion processes in lithium-sulfur batteries. *Nano Energy* **106**, 108037 (2023).

62. Lu, D. et al. Expediting stepwise sulfur Conversion via spontaneous built-in electric field and binary sulfiphilic effect of conductive NbB_2-MXene heterostructure in lithium–sulfur batteries. *Adv. Funct. Mater.* **33**, 2212689 (2023).

63. Zhang, S. et al. Palygorskite-derived ternary fluoride with 2D Ion transport channels for ampere hour-scale Li-S pouch cell with high energy density. *Adv. Mater.* **36**, 2307651 (2024).

64. Ma, C. et al. Engineering Fe–N coordination structures for fast redox conversion in lithium–sulfur batteries. *Adv. Mater.* **33**, 2100171 (2021).

65. Zhang, Y. et al. Sauna" Activation toward Intrinsic lattice deficiency in carbon nanotube microspheres for high-energy and long-lasting lithium–sulfur batteries. *Adv. Energy Mater.* **11**, 2100497 (2021).

66. Shen, J. et al. Mechanistic understanding of metal phosphide host for sulfur cathode in high-energy-density Lithium-Sulfur batteries. *ACS Nano* **13**, 8986–8996 (2019).

67. Wang, J. et al. Engineering the conductive network of metal oxide-based Sulfur Cathode toward efficient and longevous lithium–sulfur batteries. *Adv. Energy Mater.* **10**, 2002076 (2020).

68. Sun, W. et al. Rational construction of Fe_2N@C yolk-shell nanoboxes as multifunctional hosts for ultralong lithium-sulfur batteries. *ACS Nano* **13**, 12137–12147 (2019).

69. Zeng, Z., Li, W., Wang, Q. & Liu, X. Programmed design of a lithium–sulfur battery cathode by integrating functional units. *Adv. Sci.* **6**, 1900711 (2019).

70. Fang, Z. et al. Mesoporous carbon nanotube aerogel-sulfur cathodes: A strategy to achieve ultrahigh areal capacity for lithium-sulfur batteries via capillary action. *Carbon* **166**, 183–192 (2020).

71. Zhou, G., Paek, E., Hwang, G. S. & Manthiram, A. Long-life Li/polysulphide batteries with high sulphur loading enabled by lightweight three-dimensional nitrogen/sulphur-codoped graphene sponge. *Nat. Commun.* **6**, 7760 (2015).

Author contributions

M.G.L. proposed and guided the work as principal investigator. R.Y. and M.G.L. worked on conceptualization and methodology. R.Y. performed the experimental studies and data analysis and wrote the initial draft of the manuscript. Y.C., Y.P., H.L., and Y.H. worked on materials characterization. M.K. and C.K.W.L. worked on visualization. A.T., F.T., and T.L. participated in the revision and discussion of the manuscript. All authors discussed, revised, and finalized the manuscript.

Competing interests

The authors declare no competing interests.

Additional information

Supplementary information The online version contains supplementary material available at https://doi.org/10.1038/s41467-025-57755-0.

Correspondence and requests for materials should be addressed to Mitch Guijun Li.

Peer review information *Nature Communications* thanks the anonymous reviewer(s) for their contribution to the peer review of this work. A peer review file is available.

Reprints and permissions information is available at http://www.nature.com/reprints

Publisher's note Springer Nature remains neutral with regard to jurisdictional claims in published maps and institutional affiliations.